www.DeepakPublishing.com

Richie, D., et al. (2015): JoSS, Vol. 4, No. 1, pp. 285–299
(Peer-reviewed Article available at www.jossonline.com)

www. JoSSonline.com

Photocells for Small Satellite, Single-axis Attitude Determination

David J. Richie and D. Michael Sobers, Jr.
Dept. of Astronautics, USAF Academy, USAF Academy, CO USA

Neo Ching Leng Frederick and Tan Chin Sian
Nanyang Technological University, Singapore

Abstract

Light-dependent resistors are an inexpensive means to measure light intensity as a function of incidence angle. Also known as photocells, these sensors have a long history of use in terrestrial applications such as automatic control of street lights. Since their output varies with incidence angle, they may also be used to measure a body's orientation with respect to a light source. This property, with their low cost and simplicity, makes them attractive candidates for use on small satellites. However, with low cost comes an increased need for calibration accuracy and computational rigor. This paper seeks to apply calibration and computational rigor to the use of photocells on small satellites by implementing such a system on the Air Force Academy's EyasSat[3] classroom satellite demonstrator, which has photocells on all sides. Five algorithms for determining single-axis attitude are explained and compared. These algorithms include a sinusoidal curve fit, a tangent fit, as well as methods that use least-squares linear regression to reduce calibration error. The algorithms are applied to experimental data using the EyasSat[3], resulting in single-axis attitude estimation error ranging from 1.8° to 3.5°.

1. Introduction

From the dawn of civilization, man has optimized his means to travel from place to place in a given medium. Whether building sleds or rafts to transit snow-covered or water-borne areas, or avoiding obstacles with wheeled vehicles, estimating one's position and orientation has been critical for gathering food, killing game, exploring the countryside, or otherwise transporting oneself. For centuries, to achieve such mobility, people have relied on rotational and transitional position estimates through human senses coupled with evolving travel modes, from camels and horses in ancient times, to automobiles and sea-faring

Corresponding Author: David J. Richie, david.richie@usafa.edu
Publication History: Submitted – 08/06/14; Revision Accepted – 03/11/15; Published – 06/15/15

vessels after the Industrial Revolution, to submersibles and spacecraft in the Space Age. Modern applications include autonomous land, air, sea, and spaceborne vehicles, which leverage feedback control systems to do the difficult task of taking desired input and producing targeted output, controlling feedback error, and relying on effective sensing. In fact, the complexity and accuracy of such sensing equipment have evolved drastically since that time.

In spacecraft applications, this concept is inherent to determining the system's attitude via its Attitude Determination and Control Subsystem (ADCS). Primary common space attitude references include the earth (magnetometers and horizon sensors), the sun (photo-diode-based sun sensors, photo voltaic array solar panel currents, and photo-resistors), stars (star cameras and star trackers), and intrinsic inertial systems (mechanical and ring-laser gyroscopes, inertial measurement units, and rate sensors). Perhaps the most common attitude determination systems use sun sensors, due to a long heritage of photo-sensor hardware development and relatively easy access to on-orbit solar light. As addressed by Hall, the commonly used combined suite of sun sensors plus magnetometers achieves attitude estimation accuracy ranging from 1° – 5° (Hall, 2003).

Photo sensitive devices, including solar cell photovoltaics, photodiodes, and light dependent resistors (a.k.a. "photocells"), which all rely on converting light energy into electrical signals, have a rich history dating back to Becquerel's 1839 photo-voltaic work and evolving through Smith, Fritts, and Hertz' efforts in the 1870s to early 1900s (Becquerel, 1839; Smith, 1873; Fritts, 1883; Hertz, 1887; and Khan, 2004). Due to response variability and other design factors, photocells, the least expensive of these devices, found function in terrestrial street lights and warning beacons, growing into prevalence during the energy crisis of the 1970s (DOE; Adafruit; and Ladyada).

The aforementioned space age engendered the birth of satellites, small in stature at first, but growing to large behemoths for such missions as television/communications, hardened military command and control networks, and missile warning (DOE). Essentially all satellites since the late 1950s have used photovoltaic arrays for primary power and photodiode-based sun sensors in attitude determination suites (DOE). As technology has matured, satellite components have miniaturized, but mission requirements have become more demanding. This means that more is expected in smaller packages, a push that grew out of universities such as the University of Surrey in Guildford, UK, which launched wildly succesful low-cost, COTS-based systems, such as UoSat-1, UoSat-2, and its Disaster Monitoring Constellation. Adding to these small satellite successes, development of the CubeSat standard, led by Dr. Bob Twiggs in the late 1990s/early 2000s, also drove many satellite efforts to reduce satellite size, weight, and power while maintaining capability. Another key microsatellite development that occurred in parallel with CubeSat development was that of the USAF Academy's EyasSat system (Ritchey, 2004). EyasSat is a low-cost classroom demonstrator satellite developed to teach USAFA cadets to "learn space by doing space," by applying systems engineering design principles to satellites to join the USAF's "space cadre." In fact, the National Security Space Institute's Space 200 class helps teach space industry officers and mid-level professionals the ins and outs of satellite systems via EyasSat demonstrations (NSSI). The near future points to continuing this trend (Shiroma, 2011). In fact, several new countries have entered the space-faring fray, formerly reserved for a handful of countries (Hardwood).

Meanwhile, with photosensitive devices being commonplace for attitude determination, algorithms to match these approaches are in demand. Most previous algorithms have focused on photodiode-based sun sensors (Wertz, 2002; Shafer, 2008; and Lee, 2009). However, more ADCS algorithms are being used for photocell employment and also for photovoltaics doubling as small satellite sensors (Farhat, 2003; Shafer, 2008; and Martnez). Some realistic algorithm approaches, including photocell pyramid, quadrant photodiode, pinholes and lenses, CMOS sensors, and position-sensitive devices, which all seek to "centroid" the result, thus requiring more computation, have arisen from current CubeSat photosensitive options (Shafer, 2008 and Lee, 2009). Given the push for highly capable CubeSats to be available cheaply, and the fact that accurate pointing

functions are critical to meet this need, it is imperative the right sensor system is used. Even for small satellites, photodiode-based sun sensors are in the range of $10k–$20k, whereas photocell solutions are a fraction of the cost at $1–$2 each (Adafruit). Hence, there is a need to adequately investigate attitude determination algorithms for using photocells in CubeSat applications. Fundamentally, photocells are cheaper, but they require more robust computation to be on par with their photodiode brethren. In fact, preliminary work by Ritchey et al. on EyasSat demonstrated the use of simple photocells for microsatellite-class systems in 2004, albeit with key limitations in size and performance (+/– 90° accuracy).

This paper compares and contrasts several attitude determination algorithm approaches using photocells. To achieve this goal, the rest of the paper is organized as follows: Section 2 identifies the math techniques associated with five underlying algorithms investigated, defining how to scale the sensor measurements, as well as how to use them in algorithm computation. Section 3 presents the applied testing approach, heavily leveraging the work of Ritchey et al. Section 4 presents estimated slew angles and associated error for each algorithm based on a common measurement data set, and Section 5 compares and contrasts these results. Finally, Section 6 summarizes this effort's key conclusions.

2. Math Techniques

To use photocell sensors (such as those shown in Figure 1) to determine satellite attitude, one must first define a reference frame for the sensors' geometric orientation with respect to a light source. Next, preliminary governing equations are identified which relate sensor measurement to body attitude with respect to a light source. Finally, different solution algorithms can be applied to estimate body attitude from light intensity measurements, and the results can be used to evaluate the performance of each algorithm against the test data to determine suitability for in-situ space employment. This work starts with a description of the basic attitude determination configuration.

2.1. Light Source to Photocell Geometry

Figure 2 illustrates the basic geometry and associated parameters for a small satellite equipped with photocell sensors on its six contiguous faces in relation to a dominant light source. Next, assume the satellite is rotated about a single axis, in this case the Z axis. Then, each of its faces lie long the X and Y axes, respectively. In this figure, the faces are labeled "Xp" (for the +X axis), "Yp" (+Y), "Xn" (–X), and "Yn" (–Y). Each face's sensor, then, outputs a digitized resistance value in computer "counts" in-

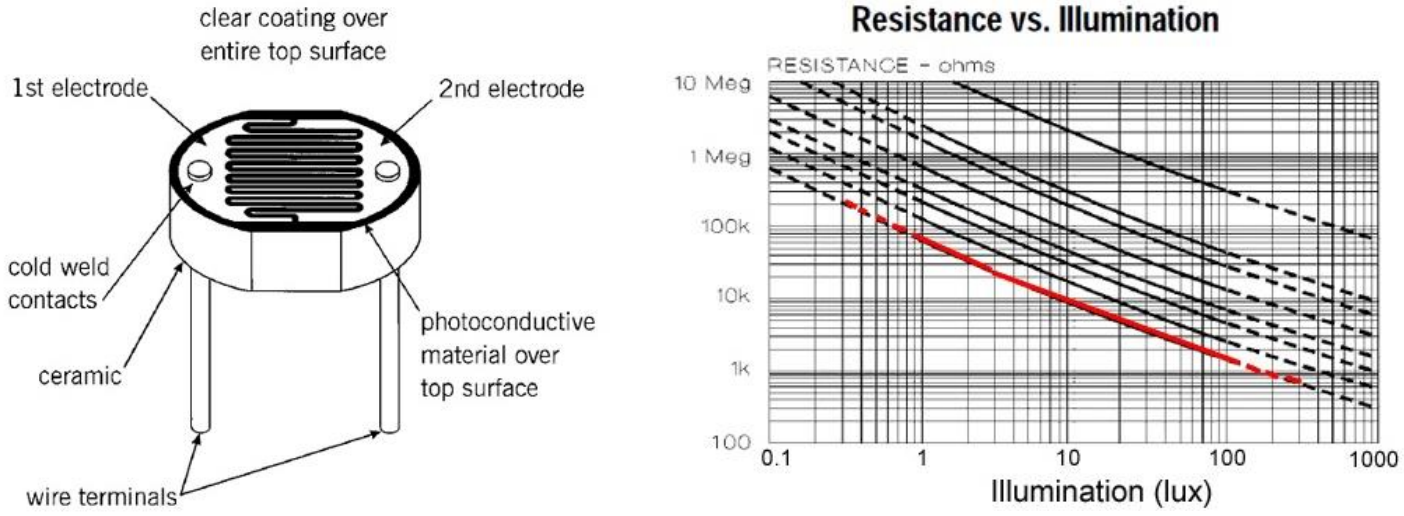

(a) *(b)*

Figure 1. Typical photocell construction (a) and response curves (b) (Adafruit).

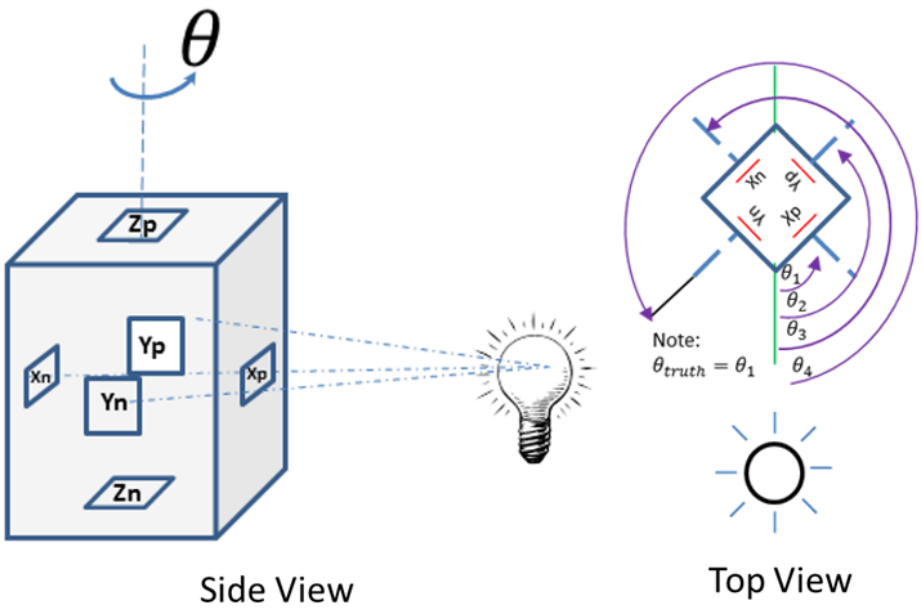

Figure 2. Side and top views for photocell single-axis measurement geometry.

versely proportional to the intensity of light on that sensor, which is itself a function of the sensor incidence angle. For example, the Xp sensor measures light resistance based on its local incidence angle, α_{x_p}, and the total satellite slew angle, θ, is measured about the rotation axis (the Z axis, in this case). Using this geometry, the five ensuing algorithms will capture different approaches for estimating the slew angle θ based on the angle measurements at Xp, Yp, Xn, and Yn. Later, the results will be compared to the true slew angle, θ_{truth}.

2.2. Preliminary Computations: Shifting and Scaling

Having defined the underlying geometry, the next step is to describe the data reduction process used to prepare the data before the angle estimation algorithms are applied. Each sensor produces a 10-bit digitized measurement from 0 to 1023, with lower resistance values (fewer counts) corresponding to higher light intensity. Since the algorithms described below begin with a trigonometric curve-fit, it is desired to scale the data to the –1 to +1 function range. To eliminate differences in sensor response, each set of sensor data is shifted and scaled as follows. First, the sensor response for each sensor over all angles is placed in a measurement column matrix, $\bar{m}$. The midpoint for each sensor data set (δ) is then calculated as shown in Eqn. 1.

Next, the scale factor (h) for each sensor is calculated using Eqn. 2. Finally, the data for each sensor is scaled and shifted to the desired range (–1 to +1) using Eqn. 3, producing a processed data set $\bar{t}$ for each sensor. Once determined, the values of δ and h for each sensor are assumed to remain constant as long as the light source intensity (and distance) remains unchanged.

$$\delta = \frac{\min(\bar{m}) + \max(\bar{m})}{2} \tag{1}$$

$$h = \max(\bar{m}) - \delta \tag{2}$$

$$\bar{t}_i = \frac{\bar{m}_i - \delta}{h}, \qquad i = 1,2,\cdots,\#\ of\ measurements \tag{3}$$

The above process can then be applied to all data collected from the sensors prior to applying the attitude estimation algorithms described on the following page. Figure 3 shows an example of the raw data collected for all four photocell sensors (Xp, Yp, Xn, Yn), and the result of processing the data as described above.

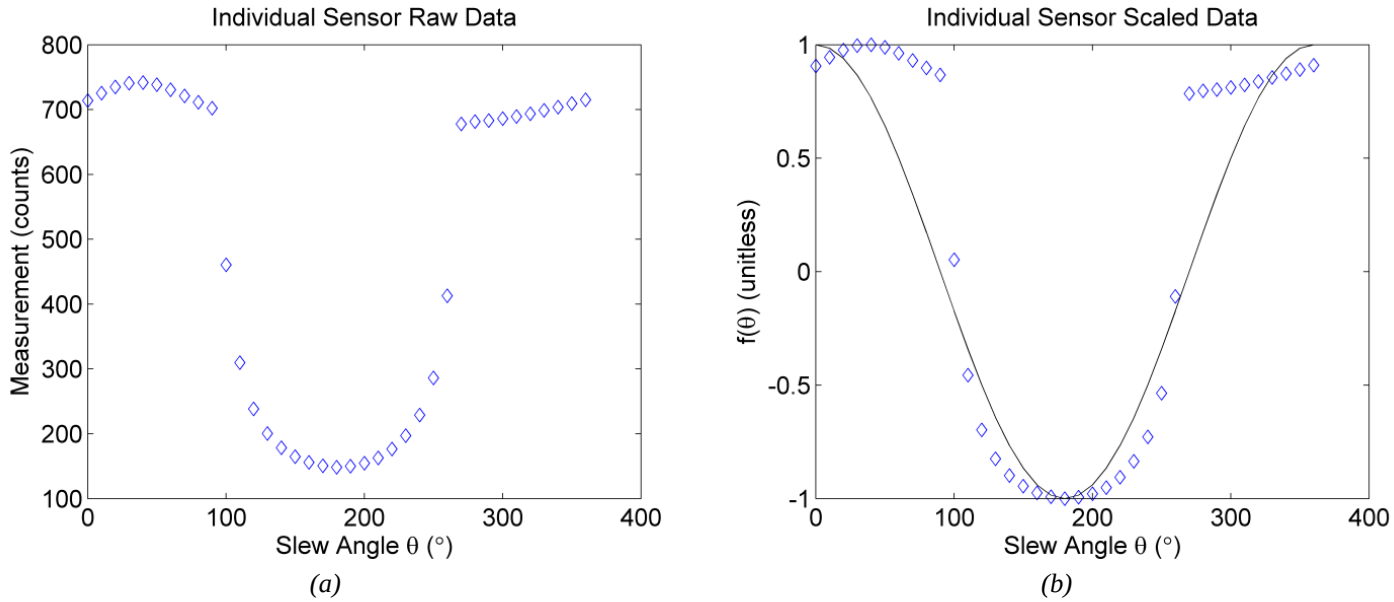

(a) *(b)*

Figure 3. From left: (a) raw measurements vs. sensor slew angle, (b) scaled measurements vs. slew angle.

2.3. Algorithm #1

Algorithm #1 uses a trigonometric function, $f(\theta_{truth})$, to fit to each sensor's scaled measurement, t_i, as given by Eqn. 4. This yields an initial guess for θ_{truth} for each sensor, $\hat{\theta}_i$:

$$\hat{\theta}_i = {f_i}^{-1}(t_i) \tag{4}$$

Figure 4 shows an example of sensor measurements t_i versus $\hat{\theta}_i$ plotted along with $f_i(\theta_{truth})$ versus θ_{truth}. In this case, the following functions are used for $f_i(\theta_{truth})$:

$$f_1(\theta) = -\cos\theta \;;\; f_2(\theta) = -\sin\theta \;;\; f_3(\theta) = \cos\theta \;;\; f_4(\theta) = \sin\theta \tag{5}$$

Using the sensor measurements to estimate the individual panel angles $\hat{\theta}_i$, the equations become:

$$\hat{\theta}_1 = {f_1}^{-1}(t_1) = -\cos^{-1}(t_1) \tag{6a}$$

$$\hat{\theta}_2 = {f_2}^{-1}(t_2) = -\sin^{-1}(t_2) \tag{6b}$$

$$\hat{\theta}_3 = {f_3}^{-1}(t_3) = \cos^{-1}(t_3) \tag{6c}$$

$$\hat{\theta}_4 = {f_4}^{-1}(t_4) = \sin^{-1}(t_4) \tag{6d}$$

These inverse trigonometric functions (i.e. for cosine and sine) range from 0 to π for cosine and $-\pi/2$ to $\pi/2$ for sine, and in each case a quadrant check must also be used to resolve ambiguity. Combining these ideas, the following functions (Eqns. 7a to 7d) were used to convert $\hat{\theta}_i$ results to the proper 0 to 2π interval, given as $\bar{\theta}_i$:

$$\bar{\theta}_1 = \hat{\theta}_1 \; for \; (t_4 \geq t_2) \quad else \quad \bar{\theta}_1 = (2\pi - \hat{\theta}_1) \tag{7a}$$

$$For \; (\hat{\theta}_2 \geq 0): \quad \bar{\theta}_2 = \hat{\theta}_2 \; for \; (t_1 \geq 0) \quad else \quad \bar{\theta}_2 = (\pi - \hat{\theta}_2)$$

$$For \; (\hat{\theta}_2 < 0): \quad \bar{\theta}_2 = (\pi - \hat{\theta}_2) \; for \; (t_1 < 0) \quad else \quad \bar{\theta}_2 = (2\pi - \hat{\theta}_2) \tag{7b}$$

$$\bar{\theta}_3 = \hat{\theta}_3 \; for \; (t_2 \leq t_4) \quad else \quad \bar{\theta}_3 = (2\pi - \hat{\theta}_3) \tag{7c}$$

$$For \; (\hat{\theta}_4 \geq 0): \quad \bar{\theta}_4 = \hat{\theta}_4 \; for \; (t_3 \geq 0) \quad else \quad \bar{\theta}_4 = (\pi - \hat{\theta}_4)$$

$$For \; (\hat{\theta}_4 < 0): \quad \bar{\theta}_4 = (\pi - \hat{\theta}_4) \; for \; (t_3 < 0) \quad else \quad \bar{\theta}_4 = (2\pi - \hat{\theta}_4) \tag{7d}$$

In this manner, the values of the sensors on other side panels are used to check that a given sensor's estimate lies in the correct quadrant, resulting in four estimates for the slew angle that lie in the interval 0 to 2π. Once the individual estimates are computed, the lit sides are used to determine the best estimated

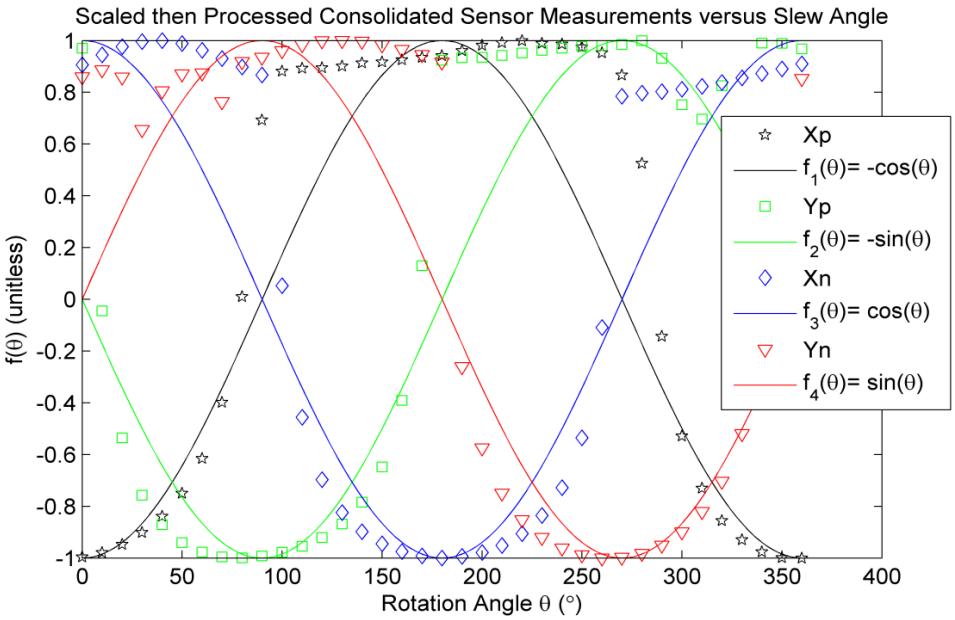

Figure 4. Example data set showing the relationship between the sensor panel angle and the Algorithm #1 trigonometric curve fit.

slew angle. This is accomplished by merging calibration data from opposite panels into sets θ_a and θ_b. If only one side is lit, θ_a or θ_b is used for the estimate. If two side panels are lit, the estimate is found using the (θ_a , θ_b) average per Eqn. 8:

$$\bar{\theta}_{est1} = \frac{\bar{\theta}_a + \bar{\theta}_b}{2} \tag{8}$$

This resulting angle, $\bar{\theta}_{est1}$, for Algorithm #1 is comparable to the true slew angle, θ_{truth}.

2.4. Algorithm #2

Algorithm #2, similar to that in Shafer et al., leverages the geometry of the previous $f_i(\theta)$ versus t_i curves, yielding a direct relationship of scaled measurement counts to estimated vehicle slew angle:

$$\frac{f_4(\theta)-f_2(\theta)}{f_3(\theta)-f_1(\theta)} = \frac{\sin\theta-(-\sin\theta)}{\cos\theta-(-\cos\theta)} = \frac{2\sin\theta}{2\cos\theta} = \frac{\sin\theta}{\cos\theta} = \tan\theta \tag{9}$$

Since most computer calculation packages (e.g., MATLAB or Microsoft Excel) have an available "atan2" function that incorporates a quadrant check directly, this function is essentially self-contained, with one caveat. The domain for atan2 is $-\pi$ to $+\pi$; thus to get a value from 0 to 2π, one must add π to the result. Eqn. 10 enables one to obtain an estimate for the slew angle directly:

$$\bar{\theta}_{est2} = \tan^{-1}\left(\frac{t_4-t_2}{t_3-t_1}\right) - \pi \tag{10}$$

Similarly to Algorithm #1, the estimated angle, $\bar{\theta}_{est2}$, for Algorithm #2 is compared to true slew angle in Section 5.

Setting the stage for the next algorithm, a least-squares linear regression analysis was performed on the total slew angle estimates for Algorithm #2. This produces a correction that uses a set of calibration measurements taken at fixed intervals around a full circle to improve the estimate produced by Algorithm #2. The linear regression correction is governed by the following equations:

$$x_i = \frac{\theta_{truth\_i}}{\Delta\theta_{truth}} \quad ; \quad y_i = \bar{\theta}_{est2\_i} \tag{11a), (11b}$$

$$\bar{x} = \frac{\sum_{i=1}^{n} x_i}{n} \quad ; \quad \bar{y} = \frac{\sum_{i=1}^{n} y_i}{n} \tag{11c), (11d}$$

$$\beta = \frac{\sum_{i=1}^{N}(x_i-\bar{x})\sum_{i=1}^{N}(y_i-\bar{y})}{\sum_{i=1}^{N}(x_i-\bar{x})^2} \quad ; \quad \alpha = \bar{y} - \beta\bar{x} \tag{11e), (11f}$$

$$y_{lin\_regress} = \alpha + \beta x_i \tag{11g}$$

Where $\Delta_{\theta_{truth}}$ is the true slew angle interval size for calibration measurements along a circle (+10° for the cases shown in Section 5). In Eqn. 11, x_i and y_i are the coordinates of the measurements when plotted on a graph of calibration angle θ_{truth_i} versus estimate $\bar{\theta}_{est2\_i}$. Also, α and β are constants, and $\bar{x}$ and $\bar{y}$ are the means of x_i and y_i, respectively. Figure 5 shows how Eqns. 11a–11g are applied to an example data set. Once the linear regression line is calculated, slew angle estimates can be corrected by subtracting the offset of the linear regression line at that angle from the line through the calibration set. Realizing that the difference between the regression line and the true slew angle line represents the algorithm's error, one can further refine this correction by dividing the linear regression into smaller pieces. This piecewise linear regression approach is applied next.

2.5. Algorithm #3

Algorithm #3 applies the aforementioned piecewise linear regression fit to improve Algorithm #2's accuracy. In other words, one estimates the slew angle via the inverse tangent method in Algorithm #2, and refines it via a piecewise linear regression process, fitting calibration curves over different intervals. Eqns. 10 and 11a–11g are key to this method. The results are illustrated in Figure 6. The associated estimated error improvements are discussed in Section 5.

2.6. Algorithms #4 and #5

Similar to the way Algorithms #2 and #3 apply linear regression to calibrate results, Algorithms #4 and #5 apply the same approach to calibrate the Algorithm #1 results. More specifically, Algorithm #4 calibrates the sets θ_a and θ_b individually using linear regression, and then combines them to get $\bar{\theta}_{est4}$, whereas Algorithm #5 calibrates the sets θ_a and θ_b using piecewise linear regression and then combines them to get $\bar{\theta}_{est5}$. Results of applying Algorithms #4 and #5 are presented in Section 5.

3. Experiment Configuration

The U.S. Air Force Academy's EyasSat[3] educational satellite demonstrator consists of a 3U CubeSat and a "hamster ball" spherical air-bearing test apparatus for demonstrating three-dimensional satellite attitude determination and control in the classroom. This system is the next evolution of the well-known

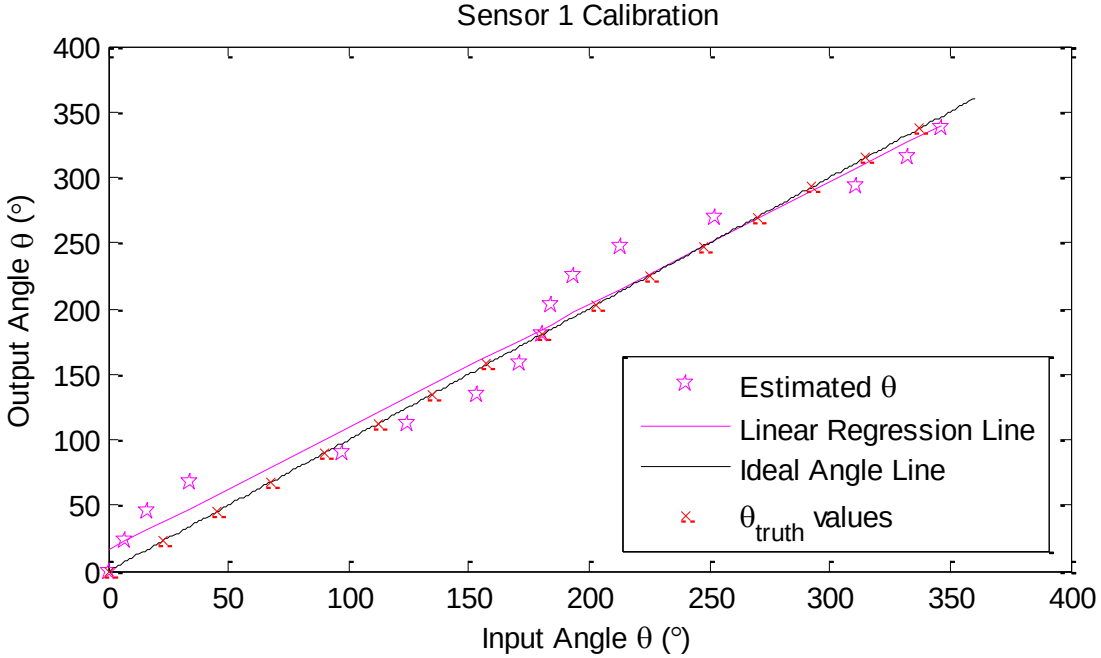

Figure 5. Algorithm #2 Tangent fit with least-squares linear regression correction as applied to sensor Xp.

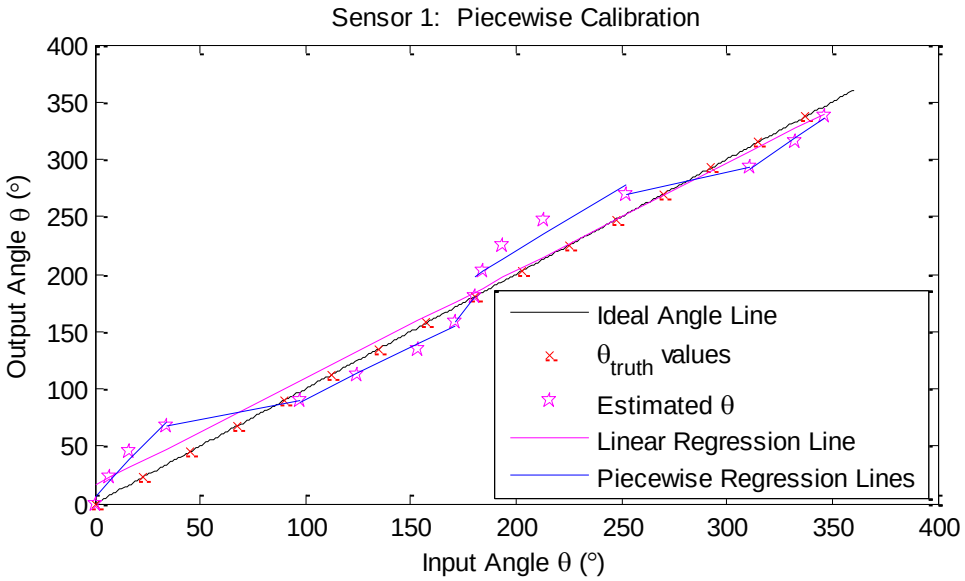

Figure 6. Algorithm #3 Tangent fit with piecewise least-squares linear regression calibration for sensor Xp.

EyasSat program with added capabilities (Sellers et al., 2013). Prior to employing the system in a three-dimensional rotational testbed, it was first necessary to assess its single-axis performance in a single-axis laboratory test using the methods described in Section 2. The test was formulated, developed, executed, and analyzed in order to demonstrate the efficacy and effectiveness of the five algorithms described above. The following discussion, which highlights key test aspects, begins by describing the satellite geometry, per side photo resistor configuration, and additional test configuration hardware and software. Test results follow in Section 4, with analysis in Section 5.

3.1. Sensor Location, Operation, and Data Collection

EyasSat[3] employs Light Dependent Resistor (LDR) photocells on each side of the bus, as shown in Figure 7. Each sensor collects incident light falling on its surface, which affects the resistance through the photocell. The resistance of each photocell is measured via voltage drop using an analogue to digital (AD) converter. The AD converter output is in measurement counts, with lower numbers indicating lower resistance due to higher incident light falling on a particular sensor. These measurements are then calibrated and combined using the methods described in Section 2 to determine three-dimensional orientation with respect to a light source.

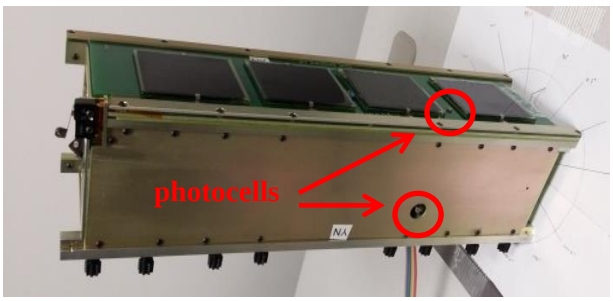

(a)

(b)

Figure 7. The EyasSat[3] bus (a) has a photocell (b) on each face.

3.2. Experiment Configuration and Logic Flow

The test configuration shown in Figure 8 shows the EyasSat[3] positioned on a table at a fixed distance from a light source. The EyasSat[3] is positioned with respect to a set of reference angles so that the true slew angle with respect to the light source (θ_{truth}) can be recorded with each sensor measurement. The photocells are located on each face according to the illustration in Figure 2, with individual sensor-based rotation angles (θ_1, θ_2, θ_3, θ_4), and total vehicle slew angle, $\theta = \theta_{truth}$. Figure 8 shows the test hardware in action, with the halogen light shining on EyasSat[3] in front of a dark background to reduce stray light. This test configuration was not only used to calibrate each individual sensor, but it also helped demonstrate the true single-axis slew angle estimation algorithms presented in Section 2.

3.3. Photocell Sensor Response

To understand the error associated with the low-cost photocell sensors, an analysis was done for all of the photocells on the EyasSat[3]. The output from each photocell was recorded at incidence angles from –90° to +90° at 10° intervals. At each angle, the output was recorded thirty times, and the average and standard deviation were calculated. As seen in Figure 9, the sensors have similar response curves, but each has a unique scale factor. Calculating the scale factor using the technique described in Section 2.2 via Eqns. 1–3 allows the sensors to be compared using the same trigonometric function. Experimental results show that the photocell standard deviation varies with incident light, as shown in Figure 10, with an average standard deviation of 0.54 measurement counts. The maximum standard deviation observed was 1.07 counts at the maximum incidence angle, while the minimum standard deviation of 0.25 counts occurred near an incidence angle of 0°. This means that the sensors are most precise near the flattest part of the incident light response curve, where the light intensity is the brightest.

4. Measurement Results and Data Reduction

Data collected during the tests described in Section 3 and processed through the algorithms defined in Section 2 are summarized in Table 1. This data includes the estimated slew angle (θ_{est}) for each method, the true slew angle (θ_{truth}), as well as the angular error, calculated by $|\theta_{truth} - \theta_{est}|$.

To compare the different algorithms as discussed in Section 5, one must first understand how each slew angle estimate was computed in light of Section 2's

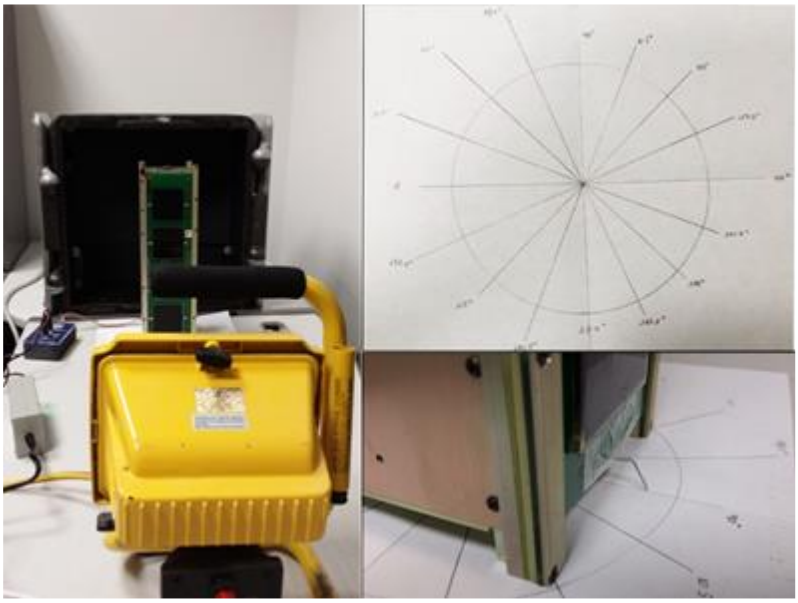

Figure 8. EyasSat[3] test setup.

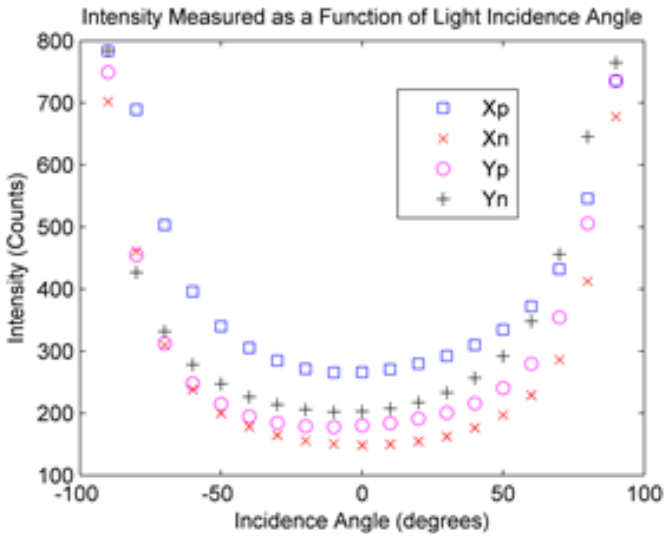

Figure 9. The photocell response curve as a function of light incidence angle. Note that lower counts correspond to higher light intensity.

algorithms. The methods to estimate slew angle for Algorithm #1, which uses the combined opposite panel curve fit, and Algorithm #2, which uses the tangent fit with linear regression, are straightforward for the methods presented in Section 2. However, for the other three methods, one must understand how these estimates are derived; in the cases of Piecewise Linear Regression (Algorithms #3 and #5), it is important to understand how the resulting estimates were found from overlapping end points from each interval. For the latter part, the steps were to obtain estimates at each interval end point; where end points overlapped between intervals, these estimates were averaged to avoid dominance of the end point sets (since each true slew angle tested was spaced out in 10° increments). Hence, the real question is how one estimates rotation angles from linear regression results. Given the α and β values for each regression interval, the estimated value for a given linear regression interval is:

$$\theta_{est_{a:b}} = \alpha + \frac{\beta\left(\theta_{truth_{a:b}} + 10^{\circ}\right)}{10^{\circ}} \quad (13)$$

where a is the lower index and b is the upper index for the slew angle interval used. The constants α and β come from the fit approach presented earlier. Once these estimates are made, the previously explained averages are used.

Table 1 includes the true slew angles, each method's estimated angular values, and the associated

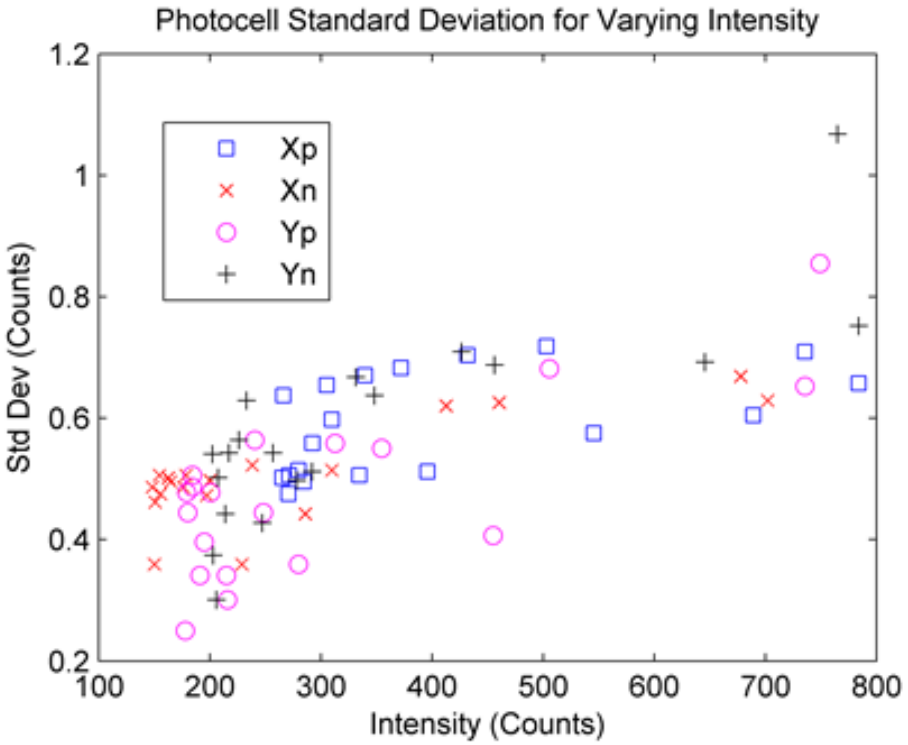

Figure 10. The standard deviation for the photocells varies by incident light intensity.

Table 1. Single-Axis Attitude Determination Algorithm Comparison

	Algorithm 1		Algorithm 2		Algoritm 3		Algoritm 4		Algorithm 5	
θ_{truth} (°)	θ_{est1} (°)	err (°)	θ_{est2} (°)	err (°)	θ_{est3} (°)	err (°)	θ_{est4} (°)	err (°)	θ_{est1} (°)	err (°)
0	1.35	1.35	4.01	4.01	7.38	7.38	1.4	1.4	0.59	0.59
30	37.46	7.46	32.39	2.39	29.04	-0.96	35.40	5.40	34.05	4.05
60	64.94	4.94	61.81	1.81	58.86	-1.14	62.89	2.89	65.48	5.48
90	82.74	-7.26	91.23	1.23	88.19	-1.81	80.58	-9.42	81.40	-8.60
120	123.56	3.56	120.65	0.65	120.32	0.32	121.30	1.30	117.77	-2.23
150	150.27	0.27	150.07	0.07	148.36	-1.64	148.00	-2.00	148.74	-1.26
180	180.00	0.00	179.48	-0.52	182.91	2.91	177.81	-2.19	179.31	-0.69
210	213.20	3.20	208.90	-1.10	212.34	2.34	211.13	1.13	212.24	2.24
240	238.68	-1.32	238.32	-1.68	238.17	-1.83	236.59	-3.41	240.64	0.64
270	265.74	-4.26	267.74	-2.26	269.52	-0.48	263.53	-6.47	269.04	-0.96
300	298.92	-1.08	297.16	-2.84	300.03	0.03	296.68	-3.32	300.47	0.47
330	333.50	3.50	326.57	-3.43	326.83	-3.17	331.23	1.23	329.08	-0.92

error. Table 2 shows each algorithm's average error and associated standard deviation. Taken together, both Tables provide valuable data for further analysis, as presented in the following text.

Table 2. Single-axis Attitude Determination Total Error Comparison

Alg #	Description	Average Error	Standard Deviation
1	Averaged Combined Panel Curve Fit	3.54°	2.71°
2	Tangent Fit, Linear Regression	1.80°	1.04°
3	Tangent Fit, Piecewise Regression	3.13°	3.55°
4	Averaged Combined Panel, Linear Regression	2.97°	2.54°
5	Averaged Combined Panel, Piecewise Regression	2.53°	2.21°

5. Discussion and Analysis

When one compares Section 4's results, especially the Table 2 algorithm error, it is clear that Algorithm #2 is the most accurate (with 1.80° average error and 1.04° standard deviation), and that Algorithm #1 is the least accurate (with 3.54° average error and 2.71° standard deviation). Although the other three algorithms' positions vary somewhat when rank ordered, these results are quite optimistic for classroom use, especially as compared to EyasSat's +/– 90° error (Ritchey, 2004).

Potential experiment error sources, crucial to understanding empirical data, are described next, and summarized in Table 3. Similar to the work of Shafer et al., these error sources are grouped into categories, (Test Configuration; Test Article Hardware; Test Article On-board Software; and Ground Support Equipment), and sorted by occurrence likelihood (low, medium, or high), based on mitigation measure existence and effectiveness. Such measures include statistically relevant trial replications, power off between trials, and predictable/reasonable measurement values produced. These measures exist and are effective for all the low likelihood sources; exist and are less effective for the moderate sources; and partially exist but are ineffective or vary widely for the three highly likely sources (Shafer, 2008). The latter three error sources were potential stray light presence; a non-collimated light source; and varying thermal bias due to temperature fluctuations during the test. Although room temperature and stray light were controlled to the extent possible, these factors may still have impacted the highly sensitive photocells.

While quantifying the error introduced by the sources listed in Table 3 would be difficult, data was collected for all of the sensors in the actual test

Table 3. Experimental Error Sources (Shafer, 2008)

No.	Error Type	High Likelihood	Medium Likelihood	Low Likelihood
1	Test Configuration	• Scatter light • Non-collimated light • Thermal bias	• Angle measurement accuracy	• Exhaustive calibration matrix • Imprecise test set up
2	Test Article Hardware		• Intermittent handheld light operation	• Component grounding • Photocell installation • Sensor dark sensitivity • Sensor hysteresis
3	Test Article On-board S/W			• Sample rate • Sample granularity • Memory allocation
4	Grnd Sprt Equip S/W			• Graphical user interface accuracy, measurement delay

environment in an attempt to measure the combined effect of all known and unknown error sources in the sensor response and test setup. As discussed in Section 3.3, the sensor response had an average standard deviation of less than one measurement count, meaning that the 1-σ statistical error is less than the analogue to digital quantization error for the sensor. As *a result, the sensor response and test setup error did* not contribute appreciably to the error of the algorithms, so the accuracy presented in Table 2 is primarily related to the differences in the algorithms themselves.

Having examined and identified the underlying potential sources of error associated with the results, the next logical step is to highlight the key advantages and drawbacks of the proposed algorithms, as well as additional tweaks required for CubeSat (e.g., EyasSat[3]) use. Table 4 summarizes these advantages and disadvantages.

Table 4. Single-axis Attitude Determination Algorithm Advantages/Disadvantages

Alg	Description	Advantages	Disadvantages
1	Averaged Combined Panel Curve Fit	• Intuitive • Average limits impact of a poor sensor	• Significant steps required to combined panel curve-fit sets • Data scaled, but no correction applied • Requires different quadrant checks for panel sine and cosine functions
2	Tangent Fit, Linear Regression	• Simpler than Algorithm 1 • Built in quad checks	• Linear regression adds some additional complexity compared to Algorithm 1
3	Tangent Fit, Piecewise Regression	• Improvement over Algorithm 1	• Piece-wise calibration complicated • More susceptible to errant sensor
4	Averaged Combined Panel, Linear Regression	• Simpler than Algorithms 3 and5 • Better percent error than Algorithms 1 and 3	• More complex than Algorithm 1 • Less accurate than Algorithms 2 and 5
5	Averaged Combined Panel, Piecewise Regression	• Improved accuracy of Algorithm 1 • Reduced susceptibility to errant panel	• Most mathematically complex, twice that of Algorithm 2

6. Conclusions

This paper has demonstrated the effectiveness of five different photocell-based CubeSat attitude determination algorithms by applying these methods on the USAF Academy's EyasSAT[3] classroom demonstrator. As shown, the novel linear-regression-based algorithms build off two existing approaches by averaging individual panel sensors and applying a tangent fit (via the atan2 software function) through combining panel pairs. The latter of these methods' advantage lies in its built-in quadrant check. The technique of using least-squares linear regression improved the accuracy of existing methods by applying a correction to the calibrated data. Applying piecewise linear regression had limited utility at the cost of increased algorithm complexity.

The combined panel tangent-fit algorithm with linear regression correction achieved an average angular estimation error of 1.80°, with a standard deviation of 1.04°. All of the methods attempted yielded average attitude estimation errors of less than 3.54°, with a worst case standard deviation of 3.55°. This is a significant improvement over previous photocell results (Ritchey, 2004), and is comparable to accuracy achieved by existing satellites using combined sun sensors and magnetometer for attitude estimation (Larson 1999, Hall 2003).

As a cheap, yet effective solution, these results reflect the great promise such photocell use affords to small satellites. These results are especially advantageous for classroom satellite demonstration, thereby showing tomorrow's Space Cadre the fundamentals of satellite attitude determination in a hands-on setting.

Acknowledgments

The authors would like to thank visiting researchers Johan Honnorat and Charly Joubert from L'Ecole de l'Air, the French Air Force Academy, for their tireless efforts collecting nearly 3000 EyasSat[3] photocell measurements. Using a coded replication matrix, they ensured data integrity and statistical significance. This work promises large academic dividends to three axis attitude determination. The authors also thank several USAFA Faculty and Staff members, past and present, for their helpful insights. First, Dr. Mike Holmes, now of the Air Force Research Laboratory (AFRL), provided several helpful discussions on photocell operation for small electronics applications. His command of unique photocell features, applied analysis validation, and nonlinearity resolution suggestions was truly invaluable. Meanwhile, Dr. Paul Vergez mentored the first author, and encouraged submittal based on the substance already acquired. Furthermore, Capt. Brian Crouse should be commended for his on-site mentorship of French cadets Honnorat and Joubert during a period of geographic separation, inspiring and directing them to collect accurate, high-value data. Finally, the authors respectfully acknowledge the resources and guidance given them by their leadership, including Col. Martin E. B. France, Head of the USAF Academy Department of Astronautics, and Singapore's National Technological University (NTU) Professor Kay Soon Low. Their guidance was critical to project success. In addition, a special thank you is owed to Lt. Col. David Barnhart as EyasSat[3] Program Manager, for procuring the test article hardware and software, the ground support hardware and software, and usage instructions from contractors Tom Murphy and Chuck Allen. Moreover, Lt. Col. Barnhart also provided the underlying idea and need for this work, and served as a stolid sounding board of the present results, offering suggestions to make the work more robust. Without him, this exciting task would not have taken shape.

References

Abramson, A. (1995): *Zworykin, Pioneer of Television*, Urbana, IL, University of Illinois Press.

Adafruit Industries. Available: http://www.adafruit.com/products/161 (accessed July 21, 2014).

Ashe, K. (2010): Photocell Economic History, coursework for Standford University Physics 240, Fall 2010. Available: http://large.stanford.edu/courses/2010/ph240/ashe2/ (accessed July 23, 2014.

Becquerel, A. E. (1839): On Electric Effects Under the Influence of Solar Radiation. *C. R. Acad. Sci*, vol. 9, pp. 561–567.

Bradford, A., et al. (2002): BILSAT-1: A Low-cost, Agile, Earth Observation Microsatellite for Turkey, presented at the *53rd Int. Astronautical Congr.*, Houston, TX, October 10–19, 2002, Paper no. IAC-02-IAA.11.3.02.

Carr, R. (2011): Estimating Errors Using Graphs and Taking Good Data, Laboratory Handbook, California State University, March 2011. Available: http://web.calstatela.edu/faculty/kaniol/Err-Gph-Meas-IBooklet.pdf (accessed July 12, 2014).

Department of Energy: History of Solar. Available: https://www1.eere.energy.gov/solar/pdfs/solar_timeline.pdf (accessed July 21, 2014).

Farhat, A., et al. (2003): Attitude Determination and Control for CubeSats, Worchester Polytechnic Institute Bachelor's Project, March 1, 2003.

Fisher, D. and Fisher, M. (1996): *Tube: The Invention of Television*, San Diego, Harcourt Brace and Company.

Fritts, C. (1883): On a new Form of Selenium Photo Cell. *Amer. J. of Sci.*, vol. 26 (156), pp. 465–472.

Hall, Christopher D. (2003): "Spacecraft Attitude Dynamics and Control." Lecture Notes, Chapter 4.

Hardwood, W., Current Space Demographics: Available: http://www.cbsnews.com/network/news/space/democurrent.html (accessed July 21, 2014).

Hertz, Heinrich (1962): On Effect of Ultra-violet Light Upon the Electric Discharge (9 June 1887), in *Electric Waves: Being Researches on the Propagation of Electric Action with Finite Velocity through Space*, D. E. Jones (Trans.), New York, Dover Publications, Inc.

Imgur: "The History of Solar Cell Efficiency." Available: http://imgur.com/r/energy/Wc1ss (accessed July 23, 2014).

Khan, A. (2004): Pre-1900 Semiconductor Research and Semiconductor Device Applications, presented at the 2004 IEEE Conference on the History of Electronics, Bletchley Park, UK, June 28–30, 2004.

Ladyada: "Photocells." Available: http:// www.ladyada.net/learn/sensors/cds.html (accessed July 21, 2014).

Lamb, T. (1935): Photoelectric Device, US Patent 2000642A.

Larson, W., and Wertz, J. (1999): *Space Mission Analysis and Design*, Third Edition, Boston, MA, Kluwer Academic Publishers.

Lee, C., et al. (2009), Sun Tracking Systems: A Review, *Sensors*, vol. 9, pp. 3875–3980. Available: www.mdpi/journal/sensors (accessed July 4, 2014).

Martinez, T.: COTS Adaptable Module for Attitude Determination in CUBESATs, Univ. of Hawaii College of Engineering report. Available: www.spacegrant.hawaii.edu (accessed July 4, 2014).

National Security Space Institute (NSSI): "About" and "Space 200 Course." Available: https://www2.peterson.af.mil/nssi/public (accessed July 21, 2014).

Nobel Foundation: "The Nobel Prize in Physics 1921." Available: http://www.nobelprize.org/nobel_prizes/physics/laureates/1921/ (accessed July 21, 2014).

Ohl, R. (1946): Light Sensitive Device, US Patent 2402662.

Post, M., et al. (2013): A low cost photodiode sun sensor for CubeSat and planetary micro-rover. *Int. J. of Aerospace Eng.*, vol. 13, 9 pages.

Ritchey, O., et al. (2004): EyasSAT: Creating A Progressive Workforce—Today, presented at the 2nd Responsive Space Conference, Los Angeles, CA, April 19–22, 2004.

Rose, A. (1952): Photoconductive Cells, US Patent 2582850.

Rose, A. (1956): Photocells, US Patent 2736848.

Schutzkin, P. (2002): *The Boy Who Invented Television: A Story of Inspiration, Persistence, and Quiet Passion*, Silver Spring, MD, TeamCom Books.

Shafer, I., et al. (2008): CubeSat Solar Sensor Final Report, Olin-NASA Research Group, Aug 1, 2008.

Sellers, J. and Barnhart, D. (2013): EyasSat^3: A Low-cost On-ramp for Nanosatellite Programs, presented at the AIAA SPACE 2013 Conference and Exposition, San Diego, CA, September 10–12, 2013, Paper no. AIAA-5325.

Shiroma, W., et al. (2011): CubeSats: A Bright Future for Nanosatellites, *Central European J. of Eng.*, vol. 1 (1), pp. 9–15.

Smith, W. (1873): Effect of Light on Selenium during the Passage of an Electric Current. *Nature*, February 20, 1873, p. 503.

Swartwout, M. (2009), The First One Hundred University-Class Spacecraft 1981–2008, *IEEE Aerospace and Electron. Syst. Mag.*, vol. 24 (3), pp. A-1-A-24.

Sweeting, M. (1987), UoSat-1: A review of orbital operations and results, *J. of the Inst. of Electron. and Radio Engineers*, vol. 57 (5), pp. S184-S194.

Wertz, J. (2002): *Spacecraft Attitude Determination and Control*, Boston, MA, Kluwer Academic Publishers.

Wicks, A., et al. (2000): Advancing Small Satellite Earth Observation; Operational Spacecraft, Planned Missions And Future Concepts, presented at the *14th Annu. AIAA/USU Conf. on Small Satellites*, Logan, UT, Aug. 2000, Paper No. SSC00-I-8.